Computer simulation study of liquid lithium at 470 and 843 K

Manel Canales
Departament de Física i Enginyeria Nuclear, Universitat Politècnica de Catalunya, Mòdul B4, Campus Nord, Sor Eulàlia d'Anzizu s/n, 08034 Barcelona, Spain

Luis Enrique González
Departamento de Física Teórica, Universidad de Valladolid, 47011 Valladolid, Spain

Joan Àngel Padró
Departament de Física Fonamental, Universitat de Barcelona, Diagonal 647, 08028 Barcelona, Spain
(Received 20 January 1994)

Both structural and dynamical properties of ^{7}Li at 470 and 843 K are studied by molecular dynamics simulation and the results are compared with the available experimental data. Two effective interatomic potentials are used, i.e., a potential derived from the Ashcroft pseudopotential [Phys. Lett. **23**, 48 (1966)] and a recently proposed potential deduced from the neutral pseudoatom method [J. Phys. Condens. Matter **5**, 4283 (1993)]. Although the shape of the two potential functions is very different, the majority of the properties calculated from them are very similar. The differences among the results using the two interaction models are carefully discussed.

PACS number(s): 61.20.Ja, 61.20.Lc, 61.20.Ne

I. INTRODUCTION

Molecular dynamics (MD) simulation is one of the most useful tools for the study of liquids at a microscopic level. MD results generally are more exact than those deduced from aproximate theories. Moreover, MD provides detailed information which is very difficult to obtain (in some cases it is impossible) from experiments. However, the realism of the MD findings requires the use of suitable interatomic potential models. In the case of liquid metals effective potentials including the averaged effects of the valence electrons should be considered and the pseudopotential theory is ordinarily used [1].

Although Li is the metal with the simplest electronic structure, the study of liquid Li at a fundamental level shows noticeable problems. For example, there are remarkable discrepancies between different measurements of the structure factor of liquid Li [2], which may be associated with the difficulties for the correction of experimental data. Moreover, the determination of an accurate effective interatomic potential for liquid Li is not easy and several pseudopotentials have been proposed [3]. Recent MD results have shown [4] that many equilibrium and time-dependent properties of liquid Li may be reasonably reproduced by using an interatomic potential with no adjustable parameters calculated by applying the neutral pseudoatom method (NPA) [3]. Nevertheless, theoretical calculations employing the variational modified hypernetted chain (VMHNC) aproximation have shown that the structure and thermodynamic properties of Li are also well reproduced by using an interatomic potential obtained from the Ashcroft pseudopotential [5] (in this case there is one adjustable parameter, the core radius). What is more surprising is that the shapes of the NPA and Ashcroft potentials are very different. Thus it may be expected that other properties such as the transport coefficients and the dynamic structure could be a more stringest test for the interaction potentials [3].

One of the aims of this work is to extend the preceding MD study of liquid Li at 470 K with the NPA potential by considering other properties such as the bond-angle distribution function, the structure factor at low k, the transversal current correlation functions, the density-energy and energy-energy correlation functions, and the k-dependent thermodynamic properties. This study, which has been carried out at two different thermodynamic states (T =470 K and 843 K), will allow us to perform a more complete comparison of the MD results and experimental data. Another objective of this work is to compare the results obtained with the NPA and the Ashcroft potentials in order to check if there are noticeable differences in the dynamic properties and which are closer to the experimental information.

II. EFFECTIVE INTERATOMIC PAIR POTENTIALS

The construction of interatomic pair potentials for simple liquid metals is based on the use of pseudopotentials to describe the interaction between ions and valence electrons and the application of second-order perturbation theory of a uniform electron gas—linear response theory (LRT)—in order to calculate the energy of the system. The resulting expression gives the effective pair potential as a sum of the direct Coulomb interaction between the ions and an electron mediated part, whose Fourier transform is related to the pseudopotential $v(k)$ and the response function of the electron gas $\chi(k)$,

$$\phi(r) = \frac{Z^2}{r} + \phi_{ind}(r) \ , \tag{1}$$

where

$$\phi_{ind}(k) = \chi(k)|v(k)|^2 \ . \tag{2}$$

The effects of exchange and correlation between the electrons are accounted for by the introduction of a local field factor $G(k)$ in the response function, which is then written as

$$\chi(k) = \frac{\chi^{(0)}(k)}{1 - \frac{4\pi}{k^2}[1 - G(k)]\chi^{(0)}(k)} \ , \tag{3}$$

where $\chi^{(0)}(k)$ is the response function of a noninteracting electron gas (Lindhard polarizability). A wide variety of expressions for the local field factor are available [6], but the relevant ones in this work are the local density aproximation (LDA) and the Ichimaru-Utsumi expression [7]. It should be noted that the latter satisfies all the self-consistency requirements.

In this work we consider two pseudopotentials. The first and simplest one is the well known empty core model. Its adjustable parameter, the core radius, was determined by fitting the height of the main peak of the static structure factor, as computed by the VMHNC, to the experimental one obtained by neutron diffraction [2], yielding a value of 1.44 a.u. The second pseudopotential has no adjustable parameters and is constructed using the NPA ideas, starting from the knowledge of the atomic number and the density of the system. The details can be found in [3,8], but the procedure is briefly as follows. First, the electron density displaced by an ion embedded in the electron gas is obtained using the NPA. Second, the density is smoothed so as to eliminate the core-orthogonality oscillations in the density which cannot appear with a pseudopotential. Third, a local pseudopotential is obtained that, when used within the standard LRT, reproduces the same electronic pseudodensity.

The effective pair potentials were obtained using the theory outlined above. In the case of the NPA pseudopotential we used the LDA local field factor so as to be consistent with the aproximations made in the computation of the pseudopotential. In the case of the empty core pseudopotential the Ichimaru-Utsumi expression was considered. The potentials obtained for the thermodynamic state close to the triple point are shown in Fig. 1. Note that the potentials are dependent on the density and therefore the potentials used at the other thermodynamic state are slightly different, though for the sake of clarity they have not been included in Fig. 1. In the case of the Ashcroft potential the differences are due to the density dependence of the electronic response function, whereas for the NPA potential we must add to this the density dependence of the pseudopotential. In any case, the effect of lowering the density is mainly a small deepening of the pair potential in the region of its minimum.

III. COMPUTATIONAL DETAILS

We have simulated ^{7}Li using the two potentials described in the preceding section at two different thermodynamic states, one close to the triple point (ρ = 0.044 512 Å^{-3}, T = 470 K) and the other one at a higher temperature and slightly different density (ρ = 0.041 62 Å^{-3}, T = 843 K). The first state has been chosen because it has been studied by both neutron [9,10] and inelastic x-ray [11] scattering. Neutron scattering experiments at the second thermodynamic state are now in progress [12]. Most of the calculations have been performed with 668 particles enclosed in a cubic box with periodic boundary conditions. Beeman's algorithm with a time step of 3 fs has been used for the integration of the equations of motion. The properties have been calculated from the configurations generated during a run of 10^5 equilibrium time steps after an equilibration period of 10^4 time steps. The k-dependent properties have been obtained in the k-range between 0.25 Å^{-1} and 5 Å^{-1} considering 20 and 10 different k values, respectively, in case of simulations at 470 K and 843 K. Moreover, in the special case of the NPA potential at 470 K, we have also performed an extra simulation using 1750 particles considering 10 different k values in the region between 0.185 Å^{-1} and 2.5 Å^{-1}. Finally, as mentioned below, we have also calculated the velocity autocorrelation function and the mean square displacement averaging over 10^4 configurations of a system made up of 3580 particles, in order to study the dependence of the diffusion coefficient with the size of the cubic box.

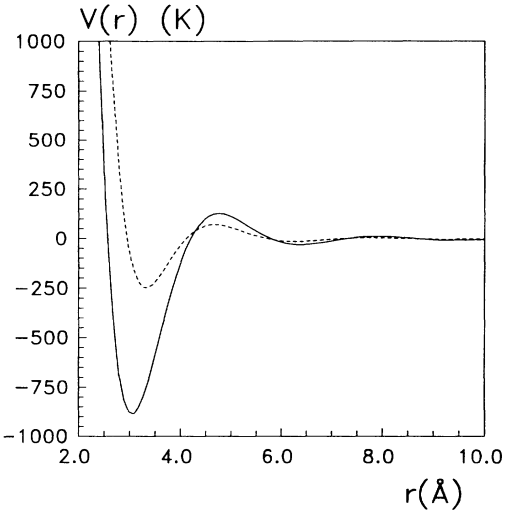

FIG. 1. Effective pair potentials $[V(r)/k_B]$ at T=470 K and ρ=0.044 512 Å^{-3}. Solid line, NPA potential; dashed line, Ashcroft potential.

IV. STRUCTURAL PROPERTIES

As we showed in a previous work [4], the structure factor $S(k)$ at 470 K calculated by MD with the NPA potential is in very good agreement with the experimental data. As expected, when the temperature increases the atoms are spread around their average positions and the peaks of the radial distribution functions $g(r)$ become lower (Fig. 2). The $g(r)$ functions obtained with the NPA and Ashcroft potentials at both temperatures are in very

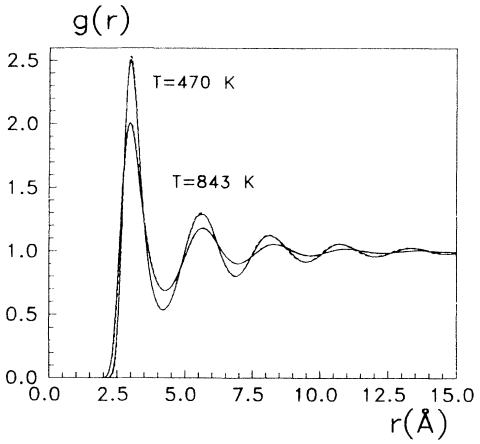

FIG. 2. Pair distribution functions at 470 K and 843 K. Solid line, NPA potential; dashed line, Ashcroft potential.

close agreement (see Fig. 2).

Although $g(r)$ is the property normally used to analyze the structure of a liquid, it is also interesting to consider higher-order structural correlation functions, which can provide more detailed structural information. The bond-angle distribution function $P(\cos\theta)$ of triplets made up of a central particle and two others located inside the first coordination shell has been used to study the local structure of dense systems [13–16]. The bond angle θ is defined as the angle between the vectors joining a central particle with the two others that make up the triplet. Then we define $P(\cos\theta)$ as the probability of occurrence of a bond angle with a cosine between $\cos\theta$ and $\cos\theta + d(\cos\theta)$. The distribution is normalized as usual:

$$\int_{-1}^{1} P(\cos\theta)\, d(\cos\theta) = 1 \ . \tag{4}$$

The bond-angle distribution function is directly related to the three-body correlation function $g^{(3)}(r, r', s)$ [13] and has the advantage of being simpler to obtain. In Fig. 3 we have plotted the bond-angle distribution functions obtained from both potentials at 470 K and 843 K. As in Lennard-Jones liquids [13,16] three peaks appear at $\theta = 55°$, 110°, and 180°. The first peak reflects the high probability of equilateral triangle configurations. The two others correspond to configurations with one or two particles, respectively, between the peripherical particles of triplets. As for $g(r)$, an increase of the temperature leads to a modification of the height of the peaks and valleys (the liquid becomes less structured), but their position is nearly the same. Figure 3 also shows that no differences can be found in $P(\cos\theta)$ as computed from either the NPA or Ashcroft potentials at both temperatures.

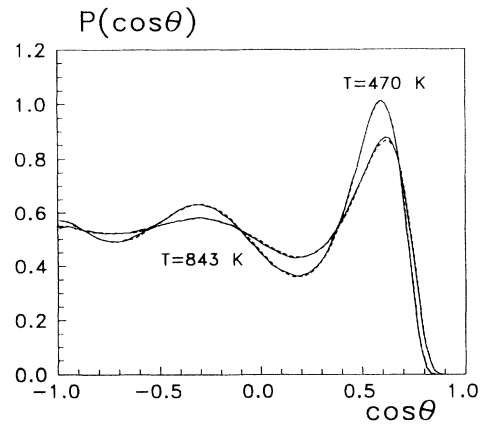

FIG. 3. Bond-angle distribution functions at 470 K and 843 K. Solid line, NPA potential; dashed line, Ashcroft potential.

V. TIME-DEPENDENT CORRELATION FUNCTIONS AND TRANSPORT COEFFICIENTS

A. Self-diffusion

The quantities normally used to describe the time-dependent properties of single particles are the normalized velocity autocorrelation function $C(t)$ and the mean square displacement $r^2(t)$, which are defined as [17]

$$C(t) = \frac{\langle \mathbf{v}(t) \cdot \mathbf{v}(0) \rangle}{\langle v(0)^2 \rangle} \ , \tag{5}$$

$$r^2(t) = \langle |\mathbf{r}(t) - \mathbf{r}(0)|^2 \rangle \ . \tag{6}$$

In Fig. 4 we have plotted the normalized velocity autocorrelation functions calculated from the NPA and Ashcroft potentials at both temperatures. In all cases a fast decay of the functions and an important backscattering that decreases when the temperature raises can be noticed. This behavior is characteristic of the $C(t)$ functions of dense liquids. The $C(t)$ obtained from both potentials are rather similar at the two temperatures. This similarity is more pronounced when we consider the

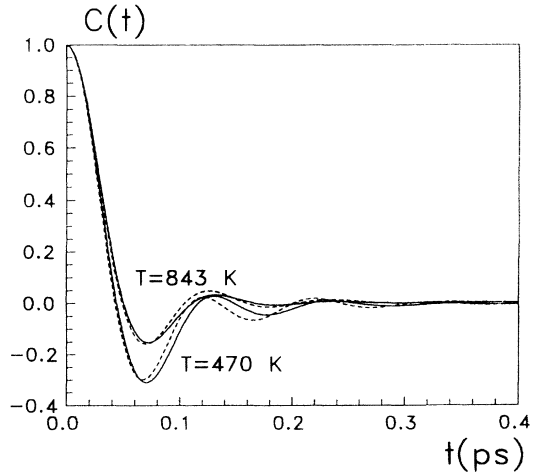

FIG. 4. Velocity autocorrelation functions at 470 K and 843 K. Solid line, NPA potential; dashed line, Ashcroft potential.

mean square displacements (Fig. 5).

The diffusion coefficient D may be obtained from $C(t)$ through a Green-Kubo relation

$$D = \frac{k_B T}{m} \int_0^\infty C(t)\, dt \ , \tag{7}$$

T being the temperature, k_B the Boltzmann constant, and m the mass of the particles. D can also be calculated by means of the Einstein relation

$$D = \lim_{t\to\infty} \frac{r^2(t)}{6t} \ . \tag{8}$$

In a previous paper [4] we simulated ^{7}Li at 470 K using a cubic box with 668 particles interacting with the NPA potential. The value for D was $(6.3 \pm 0.1) \times 10^{-5}$ cm^2 s^{-1}, which is consistent with the experimental result $(6.4 \pm 0.5) \times 10^{-5}$ cm^2 s^{-1} obtained by Murday and Cotts [18] from NMR measurements. In this work we have repeated the calculations with more care, considering a higher number of configurations and k values. The results of this more thorough analysis indicate that the most reliable value for the self-diffusion coefficient is $(6.6 \pm 0.2) \times 10^{-5}$ cm^2 s^{-1}, which is, within the error bars, consistent with the previous result and the experimental value. Moreover, we have verified that this D value is also consistent with both the decay of the self-intermediate scattering functions $F_s(k,t)$ at small k's [in this region $F_s(k,t)$ may be assumed as exponential with an exponent proportional to D] and the expected value of the half width at half maximum of $S_s(k,\omega)$ in the limit of $k \to 0$ ($\omega_{1/2}(k) \to Dk^2$) [4]. We have also studied the dependence of the diffusion coefficient with the number of particles for the NPA potential at 470 K by performing simulations with 668, 1750, and 3580 particles. The value of the diffusion coefficient has changed from 6.6×10^{-5} cm^2 s^{-1} (N=668) to $(6.9 \pm 0.2) \times 10^{-5}$ cm^2 s^{-1} (N =1750 and 3580), which is still consistent with the experimental value. The diffusion coefficients obtained with 668 particles at 470 K and 843 K are summarized in Table I. Within the error bars the D coefficients obtained from both potentials are very close and agree well with the experimental data [18,19].

B. Shear viscosity

The shear viscosity η_s is a measure of the irreversible resistance of a fluid to a change of shape. η_s can be calculated by equilibrium MD using a Green-Kubo relation from the correlations of the off-diagonal elements of the stress tensor [20,21]

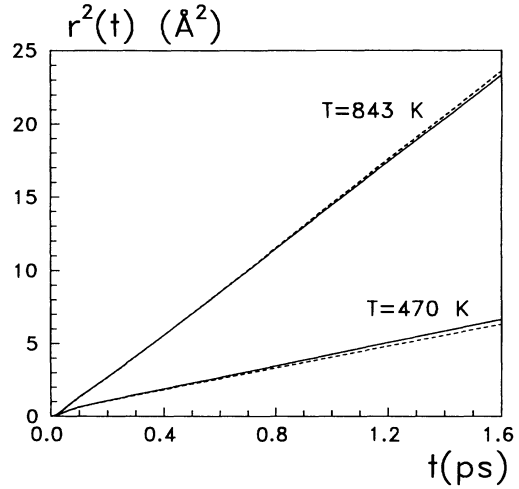

FIG. 5. Mean square displacements at 470 K and 843 K. Solid line, NPA potential; dashed line, Ashcroft potential.

$$\eta_s = \frac{1}{V k_B T} \int_0^\infty \langle J_p^{\alpha\beta}(t) J_p^{\alpha\beta}(0) \rangle dt \ , \tag{9}$$

V being the volume of the system and $\alpha, \beta = x, y, z$ with $\alpha \neq \beta$. The expression of the stress tensor elements in terms of the mass, velocities, forces, and relative distances between particles is

$$J_p^{\alpha\beta}(t) = m \sum_{i=1}^{N} v_i^\alpha(t) v_i^\beta(t) + \sum_{1=i<j}^{N} r_{ij}^\alpha(t) F_{ij}^\beta(t) \ . \tag{10}$$

The shear viscosity may also be calculated by an Einstein-like equation

$$\eta_s = \frac{V}{k_B T} \lim_{t\to\infty} \frac{L_s^2(t)}{2t} \ , \tag{11}$$

$L_s^2(t)$ being a "mean square displacement" [21], which is related to the off-diagonal elements of the stress tensor

$$L_s^2(t) = \left\langle \left[\int_0^t J_p^{\alpha\beta}(s) ds \right]^2 \right\rangle \ . \tag{12}$$

In Fig. 6 we have plotted the normalized time autocorrelation functions of the nondiagonal stress tensor

TABLE I. MD and experimental values of the diffusion (D) and shear viscosity (η_s) coefficients at 470 K and 843 K.

	470 K			843 K		
	NPA	Ashcroft	Experiment	NPA	Ashcroft	Experiment
D (10^{-5} cm^2/s)	6.6	6.3	6.4[a]	24.7	25.0	25.8[c]
η_s (10^{-4} Pa s)	5.5	5.5	5.7[b]	2.4	2.4	3.0[d]

[a]Reference [18].
[b]References [23,24].
[c]Reference [19].
[d]Reference [24].

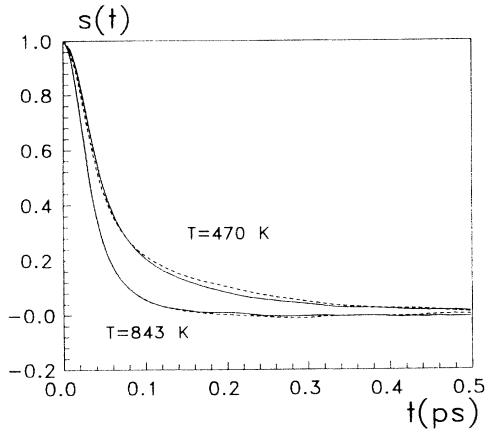

FIG. 6. Normalized time correlation functions of the nondiagonal stress tensor elements at 470 K and 843 K. Solid line, NPA potential; dashed line, Ashcroft potential.

elements $s(t)$ obtained with the NPA and Ashcroft's potentials at both temperatures. As for Lennard-Jones fluids the loss of correlation in $s(t)$ is faster when temperature increases [21,22]. The $s(t)$ results obtained from the two potentials do not show significant differences. The shear viscosity coefficients (η_s) have been computed using Eqs. (9) and (11), and the η_s values obtained by both methods have been the same. The MD findings are compared with experimental data [23,24] in Table I. The results from the NPA and Ashcroft potentials do not show significant differences and they are in reasonable agreement with the experimental data.

VI. DYNAMIC STRUCTURE FACTORS

Measurements of the coherent and incoherent cross sections in inelastic neutron scattering experiments are directly related to the dynamic structure factor $S(k,\omega)$ and its self-part $S_s(k,\omega)$, respectively. These functions are obtained as time Fourier transforms of the intermediate scattering functions $F(k,t)$ and $F_s(k,t)$, which are defined in terms of the positions of particles as [25,26]

$$F(k,t) = \frac{1}{N}\langle \rho_{\mathbf{k}}(t)\rho_{-\mathbf{k}}(0)\rangle \ , \tag{13}$$

$$F_s(k,t) = \langle e^{-i\mathbf{k}\cdot[\mathbf{r}(t)-\mathbf{r}(0)]}\rangle \ , \tag{14}$$

where $\rho_{\mathbf{k}}(t)$ is the time-dependent Fourier component of the density of the system, given by the relation

$$\rho_{\mathbf{k}}(t) = \sum_{j=1}^{N} e^{-i\mathbf{k}\cdot\mathbf{r}_j(t)} \ , \tag{15}$$

$\mathbf{k}$ being a wave vector compatible with the periodic boundary conditions [26].

In Fig. 7 the normalized $F(k,t)$ functions obtained with the NPA and Ashcroft potentials are plotted for several k values at 470 K. The only marked differences are for small wave vectors, just when the oscillatory behavior of $F(k,t)$ is important. In the case of the $F_s(k,t)$ functions we have not found noticeable differences between the results for the two potentials. The shape of the $F_s(k,t)$ functions is similar at both temperatures, but with a slower decay at 470 K. In the hydrodynamic limit ($k \to 0$) $F_s(k,t)$ has an exponential behavior [17,25]

$$F_s(k,t) = e^{-Dk^2t} \ , \tag{16}$$

where D is the diffusion coefficient. In Fig. 8 we have plotted the $-k^{-2}\ln F_s(k,t)$ function for k=0.25 Å^{-1}, obtained from the NPA potential, and the straight line using the diffusion coefficient 6.6×10^{-5} cm^2 s^{-1}, obtained

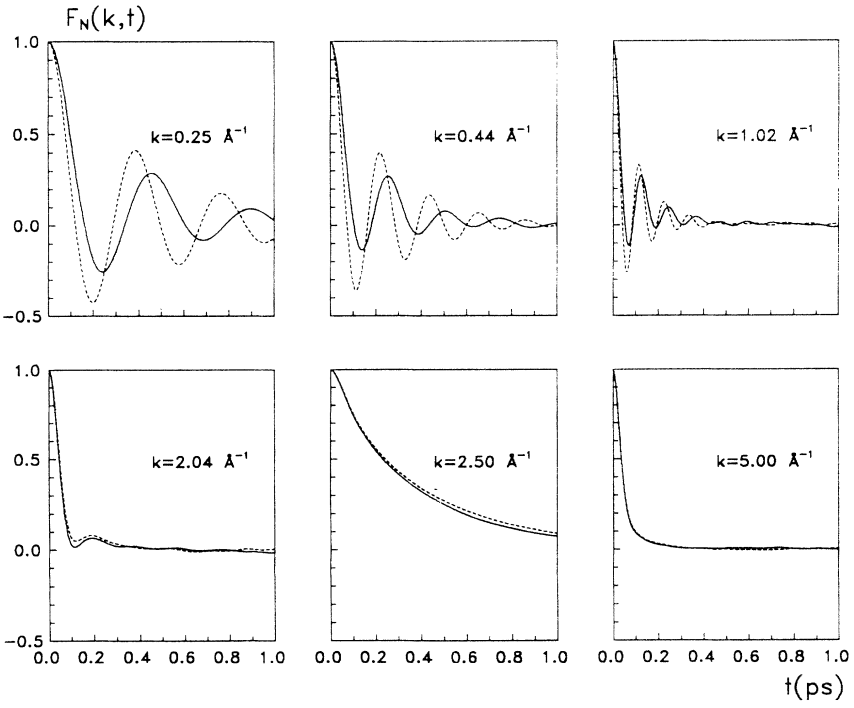

FIG. 7. Normalized intermediate scattering functions at 470 K and 843 K. Solid line, NPA potential; dashed line, Ashcroft potential.

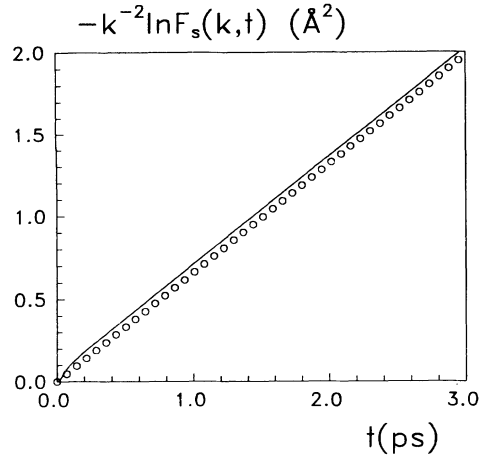

FIG. 8. Solid line, logarithm of the self-intermediate scattering function times $-k^{-2}$ for $k = 0.25$ Å^{-1} obtained from the NPA potential at 470 K; open circles, straight line using the diffusion coefficient calculated from the velocity autocorrelation function with the NPA potential.

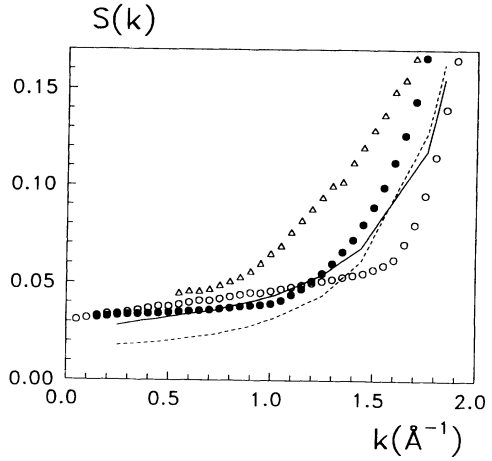

FIG. 9. Static structure factor in the small-k region at 470 K. Solid line, NPA potential; dashed line, Ashcroft potential; solid circles, Waseda data, open triangles, Olbrich *et al.* data; open circles, Ruppersberg *et al.* data. The three sets of experimental data have been taken from Ref. [2].

from the velocity autocorrelation function with the NPA potential. It should be noted that, except for a short initial decay ($t < 0.2$ ps), $F_s(k,t)$ is exponential.

The static structure factor and the intermediate scattering function are directly related by $S(k) = F(k,0)$ [17]. This allows us to calculate $S(k)$ at small-k values more exactly than if we directly determine $S(k)$ as the Fourier transform of the $g(r) - 1$ function, since $g(r)$ has been computed only up to 15 Å and the cutoff noise is important. In the literature we can find three sets of x-ray and neutron scattering measurements for $S(k)$ at T about 470 K (Waseda, Ruppersberg *et al.*, and Olbrich *et al.*). These experimental data have been compiled in Ref. [2] and they have been represented in Fig. 9 together with the MD results for $F(k,0)$. It may be noticed that the results obtained from the NPA potential are closer to the experimental data than the Ashcroft values. The isothermal compressibility (χ_T) can be obtained by means of the relation

$$\chi_T = \frac{S(0)}{\rho k_B T} , \tag{17}$$

where $S(0)$ is the static structure factor at $k = 0$, which has been evaluated from the MD results by assuming a quadratic behavior of the structure factor for small k. In Table II we have summarized the experimental and simulation χ_T values. It may be observed that the NPA results lead to values much closer to experiment [27] than the Ashcroft ones at both temperatures.

As mentioned above, the dynamic structure factors have been computed by Fourier transforming the intermediate scattering functions. In the case of $F_s(k,t)$ the time decay is very slow and the functions have only been calculated up to 3 ps. This problem is specially important for small-k values (in our case for $k < 2$ Å^{-1}). In order to circumvent this difficulty we have applied two different methods. The first one is based on the calculation of the Fourier transform of $F_s(k,t)$ extrapolated for times larger than 3 ps by assuming the exponential decay that is theoretically predicted in the hydrodynamic limit [17,25]. The second method is formally exact and can be divided in three parts. For every k value, first, the memory function $M_s(k,t)$ of $F_s(k,t)$ is computed by solving the Volterra-type equation that defines it [17,28]; afterward the Laplace transform of the memory function $\tilde{M}_s(k,z)$ is obtained. Finally, $S_s(k,\omega)$ is calculated using the Volterra equation in its Laplace form and taking into account the relation between the Fourier and Laplace transforms [17]

$$S_s(k,\omega) = \frac{1}{\pi}\mathrm{Re}\left[\frac{1}{-i\omega + \tilde{M}_s(k,\omega)}\right] . \tag{18}$$

It is important to point out that this method is feasible because $M_s(k,t)$ decreases much faster than $F_s(k,t)$,

TABLE II. MD and experimental values of the isothermal compressibility at 470 K and 843 K.

	470 K			843 K		
	NPA	Ashcroft	Experiment	NPA	Ashcroft	Experiment
χ_T (10^{-4} MPa^{-1})	0.99	0.59	1.02[a]	1.40	0.78	1.30[a]

[a]Reference [27].

being zero for times ~ 0.5 ps [$M_s(k,t)$ is approximately k^2 times the velocity autocorrelation function for small k values [17]]. Even though the first method is not exact, the results obtained using the two procedures coincide.

In Fig. 10 we have plotted $S_s(k,0)k^2$ and the half width at half maximum of $S_s(k,\omega)$ [$\omega_{1/2}(k)$] divided by k^2. The mode coupling theory of de Schepper and Ernst (SE) [29,30] predicts a linear behavior of both functions

$$\frac{\omega_{1/2}(k)}{k^2} = D(1-bk) \ , \tag{19}$$

$$k^2 S_s(k,0) = \frac{1}{\pi D}(1+ak) \ , \tag{20}$$

where D is the diffusion coefficient and a and b are parameters which can be obtained theoretically from basic quantities and from the diffusion and shear viscosity coefficients. Figure 10 shows a linear decrease of $\omega_{1/2}(k)k^{-2}$ at both temperatures and a linear increase of $S_s(k,0)k^2$ with k at 843 K, but the linear increase predicted by the SE theory does not appear for the lower temperature. The a and b values obtained both theoretically and by a least-squares fitting of the MD simulation results with the NPA and Ashcroft potentials are compared in Table III. It should be noted that the MD values of b at 470 K are in agreement with the experimental neutron scattering findings [9]. The SE predictions are consistent with the MD results at 843 K. However, Kahl *et al.* [31] analyzed their MD results for liquid lithium at 470 K using the mode coupling formalism of Wahnström and Sjögren (WS) [32] which predicts a quadratic decreasing behavior of $\omega_{1/2}(k)k^{-2}$ with k at small-k values. Our MD results can also be reasonably fitted to the WS model and the good agreement for the b parameter of the SE theory can be just accidental. Besides, as we have mentioned before, the behavior of $S_s(k,0)k^2$ at 470 K is in disagreement with the SE results, but the WS model predicts an initial decrease of $S_s(k,0)k^2$ with k, which is in a qualitative agreement with our MD findings at 470 K. The SE theory [29,30] is based on the coupling between diffusive (single particle motion) and viscous modes. On the other hand, the WS model has been constructed considering the coupling between the single particle motion and the collective density fluctuations that is especially strong at temperatures close to the melting point. Therefore, the failure of the SE theory at 470 K can be attributed to a lack of coupling between the single particle motion and the viscous mode for a liquid near the melting point, just when the cage effects are

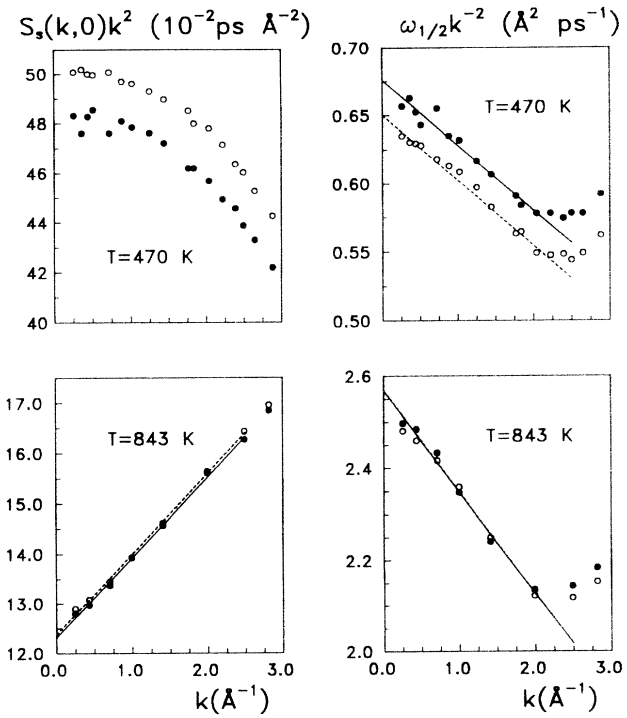

FIG. 10. $S_s(k,0)$ times k^2 and half width at half maximum $\omega_{1/2}(k)$ times k^{-2} at 470 K and 843 K. Solid circles, NPA potential; open circles, Ashcroft potential; solid line, least-squares fitting for the NPA potential results; dashed line, least-squares fitting for the Ashcroft potential results.

significant and the coupling between the diffusive mode and the collective density fluctuations is important. The agreement between the SE theory and our MD data at 843 K can be explained considering the decreasing of the cage effects when the temperature increases (the negative minimum of the velocity autocorrelation function of Fig. 4 is less pronounced at 843 K), which gives rise to a more important contribution of the coupling between diffusive and viscous modes.

$S(k,\omega)$ has been computed using a window function that removes the cutoff noise in the Fourier transform of $F(k,t)$. In order to preserve the moments of $S(k,\omega)$, the window function has been chosen constant for small times and slowly decaying up to zero at the last considered point of $F(k,t)$. This procedure renders well behaved structure factors, although it introduces the well known effects of broadening and somewhat lowering the peaks. The $S(k,\omega)$ results obtained with the two potentials at 470 K are plotted in Fig. 11. For small-k

TABLE III. Theoretical, MD, and experimental neutron scattering values for the a and b coefficients of the mode coupling theory of de Schepper and Ernst [29,30] at 470 K and 843 K.

	470 K				843 K		
	NPA	Ashcroft	Experiment	Theory	NPA	Ashcroft	Theory
a (Å)				0.10	0.13	0.13	0.21
b (Å)	0.07	0.07	0.07[a]	0.04	0.09	0.08	0.11

[a]Reference [9].

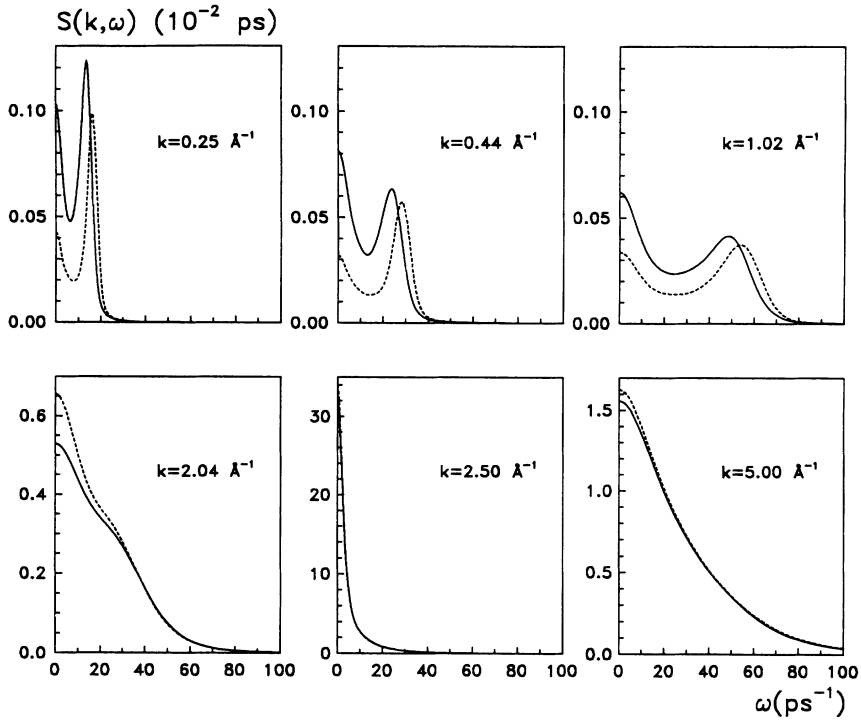

FIG. 11. Dynamic structure factors for different k values at 470 K. Solid line, NPA potential; dashed line, Ashcroft potential.

values the $S(k,\omega)$ functions corresponding to the NPA potential show higher Rayleigh and Brillouin peaks and smaller Brillouin frequencies than those corresponding to the Ashcroft potential. However, for larger-k values ($k \geq 2.5$ Å^{-1}) the results for both potentials are very similar. We have also studied the change of $S(k,\omega)$ with the temperature. Even though it is not plotted, we have seen that an increase of the temperature leads to a rise in the height of the Rayleigh and Brillouin peaks and a decrease of the Brillouin frequencies at small-k values. For larger-k values ($k \geq 2.5$ Å^{-1}) we have observed that the Rayleigh peaks at 470 K are higher than at 843 K.

The adiabatic sound velocity values c_s have been computed by a least-squares fitting of the Brillouin frequencies up to 1 Å^{-1}. The c_s results obtained using the two potentials at both temperatures and the experimental values calculated from the adiabatic compressibility data [27] are shown in Table IV. The c_s values computed from the NPA potential agree much better with the experimental results than those obtained from Ashcroft's potential, especially at 843 K where the difference is only about 2.5%. It should be pointed out that the agreement of c_s between experiments and simulations is not bad since even the smallest-k value considered in the simulations is still far from the hydrodynamic region.

Neutron scattering [9,10] and simulation results for the total dynamic structure factor $S_{total}(k,\omega)$, obtained with the two potentials at 470 K, are compared in Fig. 12. $S_{total}(k,\omega)$ is defined by

$$S_{total}(k,\omega) = \left(\sigma^i + \sigma^c\right)^{-1} \left[\sigma^i S_s(k,\omega) + \sigma^c S(k,\omega)\right] , \tag{21}$$

where $\sigma^i = 0.68$ b and $\sigma^c = 0.619$ b are the incoherent and coherent cross sections, respectively, for ^{7}Li. As shown, results obtained from both potentials are identical except for the minor differences for small-ω values at $k = 2.5$ Å^{-1}—the value of the maximum of $S(k)$—where the coherent term is greater than the incoherent part of

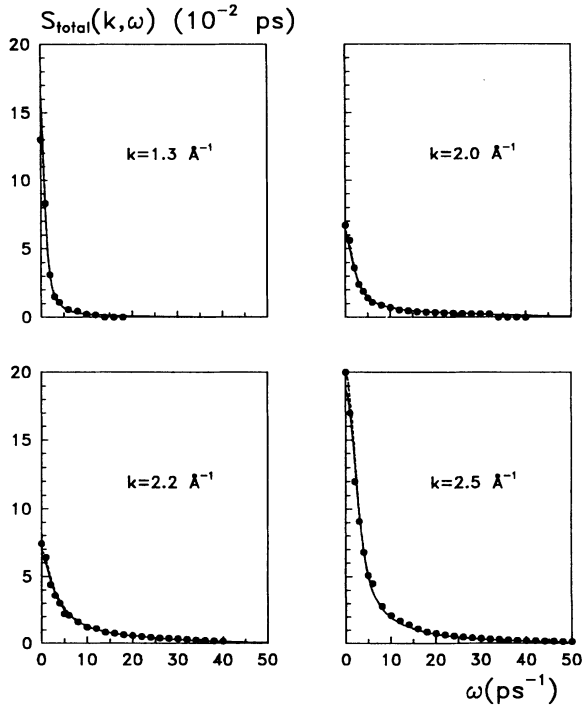

FIG. 12. Total dynamic structure factors for different k values at 470 K. Solid line, NPA potential; dashed line, Ashcroft potential; solid circles, experimental values [10].

TABLE IV. MD and experimental values of the adiabatic sound velocity (c_s) at 470 K and 843 K. MD results of the shear mode velocities (c_t) and critical wave number (k_t) at 470 K.

	470 K			843 K		
	NPA	Ashcroft	Experiment	NPA	Ashcroft	Experiment
c_s (m/s)	5250	6400	4550[a]	4300	5700	4285[a]
c_t (m/s)	3350	3250				
k_t (Å^{-1})	0.16	0.15				

[a]Reference [27].

the total dynamic structure factor. It should be emphasized that the agreement with the experimental data is excellent.

As stated in the Introduction, it was expected that the comparison of the dynamic structure factors obtained from simulations and experiments would be a suitable route to know which interaction potential produces more realistic simulations of liquid Li. Figure 12 shows that this is not the case if the experimental neutron scattering data are considered. However, the results presented in this section show that $F(k,t)$ and $S(k,\omega)$ at small k are different. Nevertheless, the neutron scattering experiments at low-k's are difficult and, what is more important, the $S_{total}(k,\omega)$ function is dominated by the incoherent contribution. Then, the experimental $S(k,\omega)$ in the low-k region must be obtained from x-ray measurements for which no incoherent scattering takes place. Liquid Li at 40 K above the melting point has been recently studied by inelastic x-ray scattering [11,33] and some of the results are compared with our MD findings in Fig. 13. In order to perform this comparison we have adapted the MD results to the experimental results according the following steps [33]: First, the MD data have been mirrored to the negative frequency region; then they have been multiplied by the detailed balance factor $e^{\hbar\omega/2k_BT}$ [17]; afterward they have been convoluted with the energy resolution function of the experimental device. Moreover, the data have been multiplied by a normalizing factor that takes into account the change of units (from ps to experimental count rates) and finally the instrumental background has been added. The agreement between the experimental and MD data is in general satisfactory, especially for the highest-k value. The only important disagreement appears for ω around 0 and $k = 0.44$ Å^{-1}. In any case, it should be noted that the differences between simulation and experiment are smaller for the NPA potential.

The sound dispersion relation $\omega_s(k)$ is determined by visual inspection of the Brillouin peak positions or Brillouin frequencies $\omega_B(k)$ of $S(k,\omega)$ for every k value. However, for sufficient large k's the Brillouin peaks are not directly visible and more sophisticated methods are required for its detection. The $S(k,\omega)$ for a simple liquid can be written according to the kinetic theory as a sum of an infinite set of Lorentzians [34]. However, for small k's, $S(k,\omega)$ can be described in terms of only three Lorentzians

$$S(k,\omega) = \frac{S(k)}{\pi}\mathrm{Re}\sum_{j=-1}^{1}\frac{A_j(k)}{i\omega + z_j(k)} , \qquad (22)$$

where A_j and z_j are either real or complex conjugate pairs. These parameters may be determined by means of a least-squares fit to the $S(k,\omega)$ result [35]. The Lorentzians triplet has one central Rayleigh line located at $\omega = 0$ that is due to the extended heat mode and two

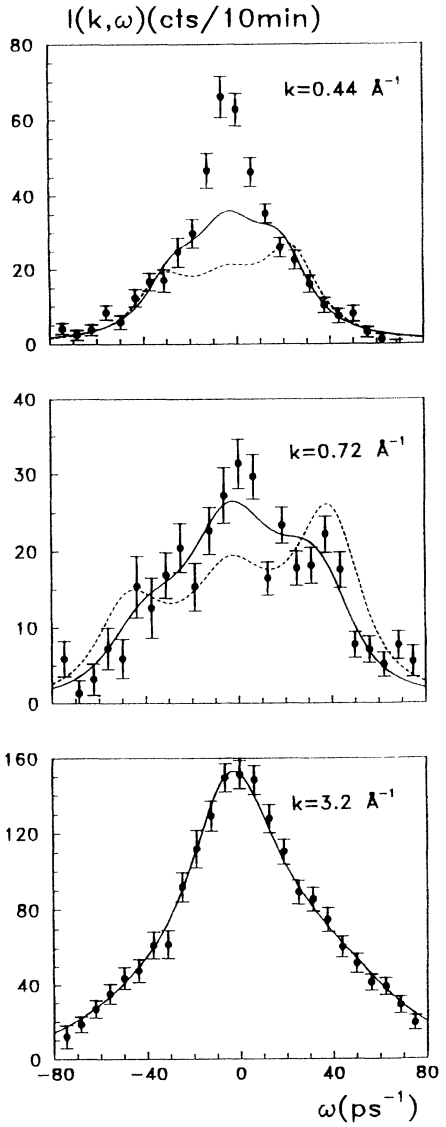

FIG. 13. Dynamic structure factors for different k values at 470 K in x-ray experimental units. Solid line, NPA potential; dashed line, Ashcroft potential; solid circles with error bars, x-ray data [11,33].

Brillouin lines located at $\omega_s(k) = \mathrm{Im}[z_1(k)]$ that are due to the two extended sound modes.

In Fig. 14 we have plotted the x-ray, the neutron scattering, and the NPA results of the sound dispersion relation at 470 K using the three Lorentzians procedure. We have also included in Fig. 14 the adiabatic sound velocity c_s straight line or hydrodynamic sound dispersion curve $\omega_s(k) = c_s k$, using the experimental sound velocity value (c_s = 4550 m/s [27]). Finally, we have plotted the theoretical results corresponding to the three Lorentzians viscoelastic model of Lovesey [17,36] computed for the NPA potential. Figure 14 shows that for small-k values there is good agreement, within the error bars, between the MD findings, the x-ray results, and the viscoelastic model predictions. Moreover, at very small k's both theoretical and experimental results approach the sound velocity limit. In the region of the largest k's ($k > 1.25$ Å^{-1}), MD results are closer to the experimental neutron scattering data than the viscoelastic model predictions.

VII. CURRENT CORRELATION FUNCTIONS

The Fourier transform of the current associated with the density of a system with N particles is given by

$$\mathbf{j}_\mathbf{k}(t) = \sum_{l=1}^{N} \mathbf{v}_l(t) e^{-i\mathbf{k}\cdot\mathbf{r}_l(t)} \ . \tag{23}$$

The longitudinal $C_l(k,t)$ and the transverse $C_t(k,t)$ current correlation functions are defined in terms of the parts of $\mathbf{j}_\mathbf{k}(t)$ which are parallel $j^{\parallel}_\mathbf{k}(t)$ and perpendicular $j^{\perp}_\mathbf{k}(t)$, respectively, to the direction of the wave vector $\mathbf{k}$

$$C_l(k,t) = \frac{k^2}{N} \langle j^{\parallel}_\mathbf{k}(t) j^{\parallel}_{-\mathbf{k}}(0) \rangle \ , \tag{24}$$

$$C_t(k,t) = \frac{k^2}{N} \langle j^{\perp}_\mathbf{k}(t) j^{\perp}_{-\mathbf{k}}(0) \rangle \ . \tag{25}$$

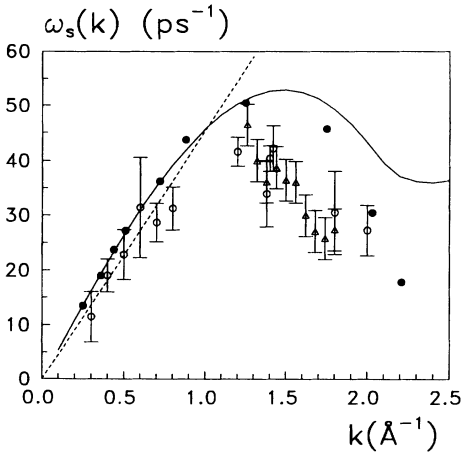

FIG. 14. Sound dispersion relation at 470 K. Solid line, Lovesey viscoelastic model [36]; dashed line, hydrodynamic sound dispersion curve; open circles with error bars, x-ray data [11]; triangles with error bars, neutron scattering data [10]; solid circles, MD results using the NPA potential.

The Fourier transforms of these functions $C_l(k,\omega)$ and $C_t(k,\omega)$ describe, respectively, the spectrum of the longitudinal (or density) and transverse (or shear) fluctuations in liquids. In order to obtain well behaved spectra, we have Fourier transformed the current correlation functions using window functions similar to those considered in the calculation of $S(k,\omega)$. In fact, the longitudinal power spectrum has been computed by two routes: first, by Fourier transforming the $C_l(k,t)$ and second, by using the equation $C_l(k,\omega) = \omega^2 S(k,\omega)$ [25]. The results obtained by both methods do not show significant differences.

In Fig. 15 we have plotted the longitudinal dispersion curves for both potentials at 470 K and 843 K. These curves have been obtained using the frequencies $\omega_l^m(k)$ corresponding to the peaks of $C_l(k,\omega)$ for different k values. We also show in Fig. 15 the Brillouin frequencies $\omega_B(k)$ corresponding to the simulation with the NPA potential obtained for small-k values by visual inspection of the Brillouin peaks and for larger k's (1.25 Å^{-1} < k < 2.5 Å^{-1}) using the three Lorentzians procedure described above. It is seen that for the smaller k's the $\omega_l^m(k)$ and $\omega_B(k)$ frequencies coincide and the shape of the dispersion curves is close to the experimental sound velocity. As k increases, $\omega_l^m(k)$ is slightly greater than the adiabatic sound velocity straight line. These may be associated with the shear relaxation effects which have also been observed for other liquid metals, both experimentally [37] and by computer simulation [26]. Finally, it should be pointed out that the longitudinal dispersion

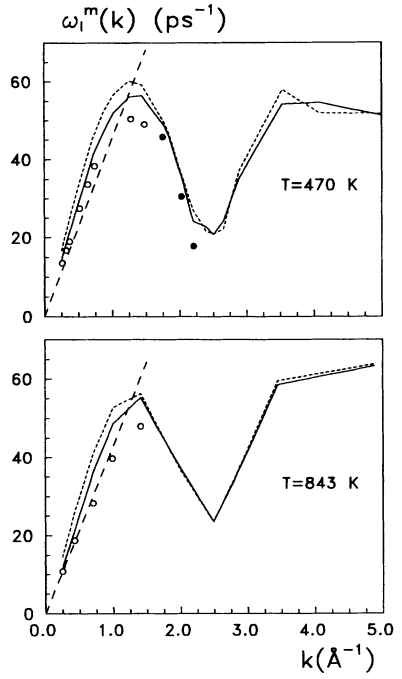

FIG. 15. Longitudinal dispersion curves at 470 K and 843 K. Solid line, NPA potential; dashed line, Ashcroft potential; long dashed line, adiabatic sound velocity; open circles, Brillouin frequencies obtained by visual inspection of the Brillouin peaks for the NPA potential; solid circles, Brillouin frequencies obtained by fitting $S(k,\omega)$ for the NPA potential to three Lorentzians.

relations corresponding to the two potentials are very close and the only noticeable differences are for $k < 1.5$ Å^{-1}.

In Fig. 16 we show the Fourier transforms of the transverse current correlation functions $C_t(k,\omega)$ at both temperatures calculated with the NPA potential for some wave vectors. At 470 K we can notice the existence of peaks at finite frequencies for all the k values considered in the figure. However, at 843 K the peaks only exist for k values longer than about 1 Å^{-1}, which reflects the difficulties for the propagation of shear waves in liquids at high temperatures. The results for the Ashcroft potential are not shown in the figure because they are almost indistinguishable from the NPA ones.

The dispersion curves of the transverse (or shear) modes, obtained from both potentials at 470 K and 843 K, are plotted in Fig. 17. These curves represent the frequency corresponding to the $C_t(k,\omega)$ peak $\omega_t^m(k)$ for every wave vector. If a linear behavior is assumed $\omega_t^m(k) = c_t(k - k_t)$ [38], the dispersion curves in the region of small wave vectors allow us to determine the velocity of the shear modes c_t and the wave vector k_t from which shear waves are supported. The c_t and k_t values obtained by a least-squares fitting at 470 K are shown in Table IV, where it can be noticed that c_t is smaller than c_s. The quotient value for the NPA potential is $c_t/c_s = 0.64$. These findings are consistent with the results obtained for other monoatomic liquids (Na, K, and Ar) near the triple point and also with the measured velocities of longitudinal and transverse sound in a variety of monoatomic solids [38].

The viscoelastic model for the transverse current correlation functions predicts that shear waves will appear

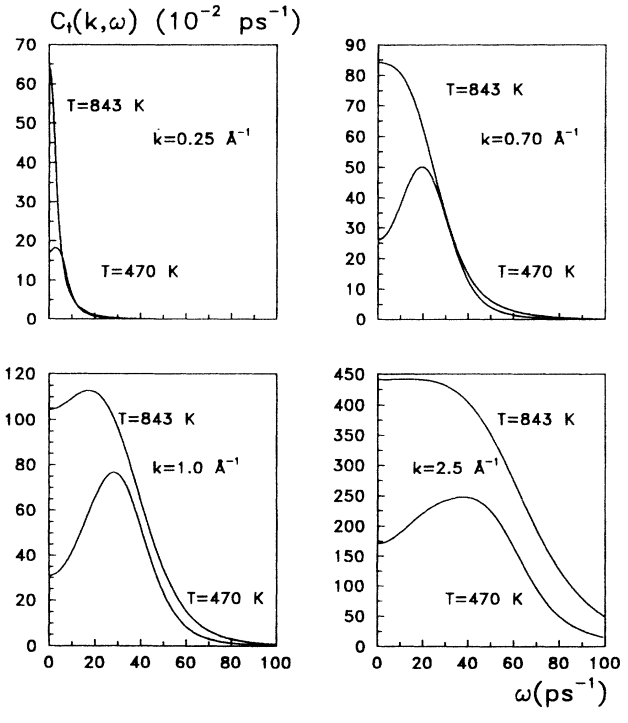

FIG. 16. Transverse current correlation functions at 470 K and 843 K calculated from the NPA potential for different k values.

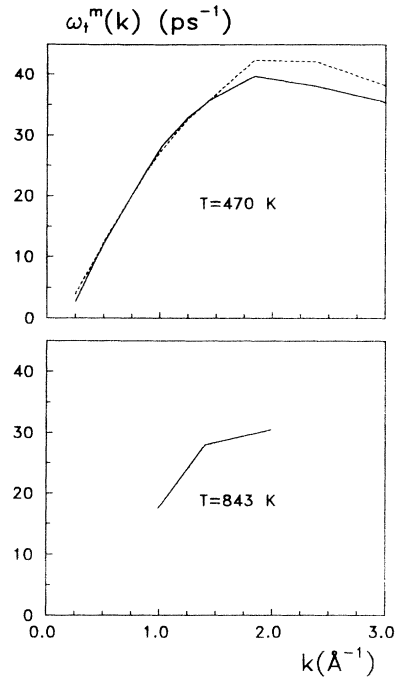

FIG. 17. Transverse dispersion curves at 470 K and 843 K. Solid line, NPA potential; dashed line, Ashcroft potential.

for values of k greater than k_c, where k_c is a critical wave vector given by [17]

$$k_c = \tau_t^{-1}(k)\sqrt{\frac{\rho m}{2G_\infty(k)}}\ , \tag{26}$$

ρm being the mass density of the system and $G_\infty(k)$ the k-dependent shear modulus. $G_\infty(k)$ is directly related to the second moment of the transverse current correlation function, which can be evaluated from the $g(r)$ and the second derivative of the potential. $\tau_t(k)$ is the exponential coefficient or characteristic time decay of the first memory function of every $C_t(k,t)$. The k_c value can be estimated by taking the k=0 limit of Eq. (26):

$$k_c \simeq \frac{1}{\eta_s}\sqrt{\frac{1}{2}\rho m G_\infty(0)}\ , \tag{27}$$

η_s being the shear viscosity coefficient.

The k_c estimated values are 0.23 Å^{-1} at 470 K and 0.49 Å^{-1} at 843 K. This last k_c value disagrees with the MD result (the first k value from which we have seen shear modes at 843 K is 1 Å^{-1}). However, at 470 K the viscoelastic estimate agrees with the MD findings (we have seen shear modes for $k = 0.185$ Å^{-1}), which are also coincident with the k_t wave vector predictions of Jacucci and McDonald [38]. From the analysis of MD results for monoatomic liquid metals (Na and K) near the triple point, Jacucci and McDonald predicted that shear modes appear from $\frac{2\pi}{14a}$ onward, where a is the nearest neighbor distance (for lithium $a = 2.5$ Å and then $k_t = 0.18$ Å^{-1}). In the same work Jacucci and McDonald also derived a formula for k_l the wave vector from which longitudinal modes dissapear ($k_l = \frac{2\pi}{1.4a}$, in our case $k_l = 1.8$ Å^{-1}).

This prediction is also close to the MD results (we have not seen a clear Brillouin peak from $k = 2$ Å^{-1} at 470 K).

VIII. ENERGY-DENSITY AND ENERGY-ENERGY CORRELATION FUNCTIONS

The basic quantities involved in the hydrodynamic model of a fluid are the microscopic density fluctuations ρ, the microscopic longitudinal velocity fluctuations u, and the temperature fluctuations T [17,39]. An equivalent description can be obtained if we substitute the temperature fluctuations by the energy fluctuations e. The study of the correlation functions between these basic quantities is important because the transport coefficients and generalized thermodynamic quantities can be obtained from them. The complete set of hydrodynamic correlation functions can be computed in terms of only three independent ones, which are the density-density correlation functions defined in Eqs. (13) and (15), the energy-density $F_{e\rho}(k,t)$ correlation functions, and the energy-energy $F_{ee}(k,t)$ correlation functions. The last two are defined as [40]

$$F_{e\rho}(k,t) = \frac{1}{N}\langle E_{\mathbf{k}}(t)\rho_{-\mathbf{k}}(0)\rangle \ , \tag{28}$$

$$F_{ee}(k,t) = \frac{1}{N}\langle E_{\mathbf{k}}(t)E_{-\mathbf{k}}(0)\rangle \ , \tag{29}$$

$\rho_{\mathbf{k}}(t)$ and $E_{\mathbf{k}}(t)$ being, respectively, the time-dependent Fourier density and energy of the system. $\rho_{\mathbf{k}}(t)$ is given in Eq. (15) and $E_{\mathbf{k}}(t)$ is defined by

$$E_{\mathbf{k}}(t) = \sum_{j=1}^{N} E_j e^{-i\mathbf{k}\cdot\mathbf{r}_j(t)} \ , \tag{30}$$

where E_j is the total energy of the particle j, i.e.,

$$E_j = \frac{1}{2}mv_j^2 + \frac{1}{2}\sum_{1=l\neq j}^{N} V_{jl}(r) \ . \tag{31}$$

In Figs. 18 and 19 we have plotted, respectively, $F_{e\rho}(k,t)$ and $F_{ee}(k,t)$ computed from both potentials at 843 K. The resulting energy-density correlation functions for the two potentials have different sign because the total energy is negative when the NPA potential is used and positive when the simulation is performed with the Ashcroft potential [3]. Furthermore, the oscillatory behavior of the correlation functions at small-k values ($k < 1$ Å^{-1}) obtained from the Ashcroft potential is in contrast with the monotonic behavior of the correlation functions computed from the NPA potential. The NPA results for $F_{e\rho}(k,t)$ and $F_{ee}(k,t)$ resemble those obtained with a Lennard-Jones potential [40] whereas the Ashcroft and NPA findings are in qualitative disagreement. Finally, it should be pointed out that, as a consequence of these different behaviors, the shapes of the Fourier transforms of $F_{ee}(k,t)$ calculated from the Ashcroft potential are similar to the dynamic structure factors $S(k,\omega)$ at small k's, i.e., they show "Brillouin-like" peaks which cannot be observed in the functions computed using the NPA potential.

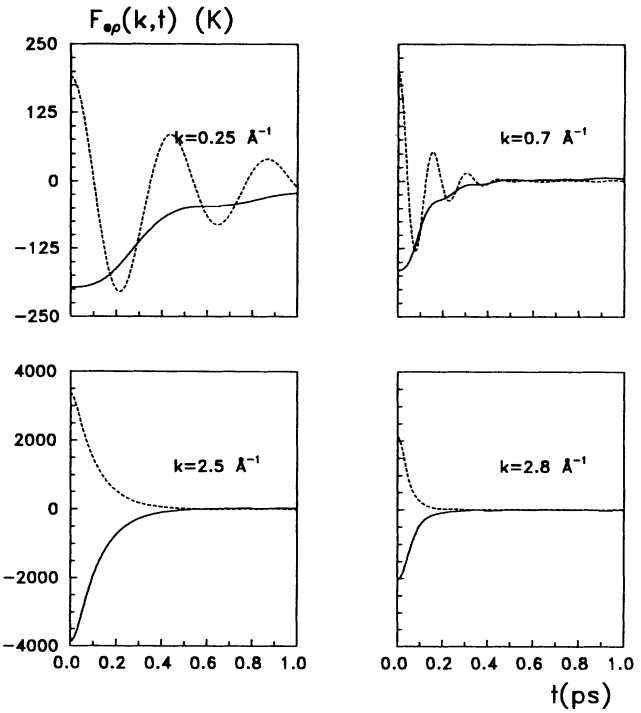

FIG. 18. Energy-density correlation functions at 843 K. Solid line, NPA potential; dashed line, Ashcroft potential.

From the correlation functions $F(k,t)$, $F_{e\rho}(k,t)$, and $F_{ee}(k,t)$ at $t = 0$ we can derive a set of generalized k-

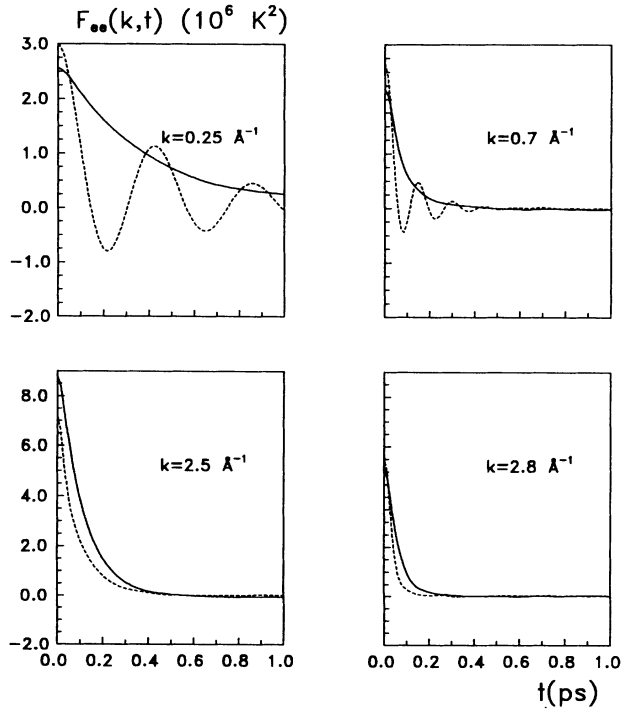

FIG. 19. Energy-energy correlation functions at 843 K. Solid line, NPA potential; dashed line, Ashcroft potential.

dependent thermodynamic quantities, which tend to the bulk thermodynamic values in the limit of $k \to 0$. The expressions for these quantities are [40]

$$h(k) = -\frac{m}{k_B T k^2} \lim_{t\to 0} \frac{\partial^2}{\partial t^2} F_{e\rho}(k,t) \tag{32}$$

for the generalized enthalpy per particle,

$$\alpha(k) = \frac{1}{k_B T^2} \left[h(k)F(k,0) - F_{e\rho}(k,0)\right] \tag{33}$$

for the generalized thermal expansion coefficient,

$$C_v(k) = \frac{1}{k_B T^2} \left[F_{ee}(k,0) - F_{e\rho}^2(k,0)/F(k,0)\right] \tag{34}$$

for the generalized specific heat at constant volume per particle,

$$C_p(k) = C_v(k) + k_B T^2 \alpha^2(k)/F(k,0) \tag{35}$$

for the generalized specific heat at constant pressure per particle, and

$$\gamma(k) = C_p(k)/C_v(k) \tag{36}$$

for the generalized ratio of specific heats.

The calculation of $h(k)$, $\alpha(k)$, $C_p(k)$, and $\gamma(k)$ is very sensitive to the numerical computation of the second derivative of the density-energy correlation function at zero time. In order to circumvent the problem we have also computed the generalized enthalpy following a more direct procedure which is based on the calculation of the energy-longitudinal momentum flux correlation function at zero time $F_{e\phi}(k,0)$ [40]

$$h(k) = \frac{m}{k_B T} F_{e\phi}(k,0) \ , \tag{37}$$

$F_{e\phi}(k,t)$ being

$$F_{e\phi}(k,t) = \frac{1}{N} \langle E_{\mathbf{k}}(t) \phi_{-\mathbf{k}}(0) \rangle \ , \tag{38}$$

where $E_{\mathbf{k}}(t)$ is defined by Eqs. (30) and (31) and $\phi_{\mathbf{k}}(t)$ is given by

$$\phi_{\mathbf{k}}(t) = \sum_{j=1}^{N} \phi_j e^{-i\mathbf{k}\cdot\mathbf{r}_j(t)} \ , \tag{39}$$

ϕ_j being the longitudinal momentum flux of the particle j, i.e.,

$$\phi_j = \left(\frac{\mathbf{v}_j \cdot \mathbf{k}}{k}\right)^2 + \frac{i}{2mk^2} \sum_{1=l\neq j}^{N} \mathbf{k} \cdot \frac{\partial V_{jl}}{\partial \mathbf{r}_{jl}} \left(e^{i\mathbf{k}\cdot\mathbf{r}_{jl}} - 1\right) \ . \tag{40}$$

The generalized k-dependent thermodynamic properties at 843 K calculated from the Ashcroft and NPA potentials are shown Fig. 20. Despite the great differences between the correlation functions $F_{e\rho}(k,t)$ and $F_{ee}(k,t)$ obtained from the two potentials, the k-dependent thermodynamic properties are similar and the values in the limit of $k \to 0$ are consistent with the experimental data ($\alpha = 1.97 \times 10^{-4}$ K^{-1}, $C_v = 3.655$ kJ kg^{-1} K^{-1}, $C_p = 4.177$ kJ kg^{-1} K^{-1}, and $\gamma = 1.143$) [27]. Moreover, in agreement with the results for Lennard-Jones systems [40], we can observe peaks in the $\alpha(k)$, $C_p(k)$, and $\gamma(k)$ curves for the k value corresponding to the $S(k)$ maximum. We have also calculated the energy-energy and the energy-density correlation function and all the thermodynamic properties at 470 K for both potentials. In all cases we have obtained the same qualitative results as for 843 K.

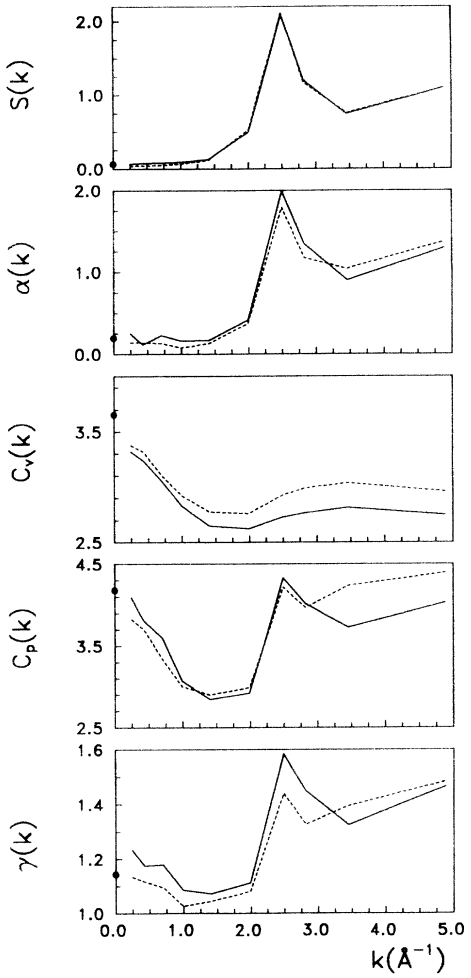

FIG. 20. Generalized k-dependent thermodynamic properties at 843 K. Solid line, NPA potential; dashed line, Ashcroft potential; solid circles, bulk thermodynamic experimental values [27]. $\alpha(k)$ and the heat specific capacities are expressed in 10^{-3} K^{-1} and kJ kg^{-1} K^{-1}, respectively.

IX. CONCLUSIONS

In this paper a wide variety set of properties of liquid ^{7}Li at two very different temperatures using two different potentials have been calculated by MD. These MD results

together with those in [4] are in reasonable agreement with the available experimental data. This corroborates that classical MD simulations using suitable effective potentials can provide realistic pictures of the microscopic behavior of this liquid.

Despite the marked differences between the two potentials used in the MD simulations, both the structural and dynamical properties calculated from the two potentials are in general very similar. Small differences have been found for χ_T and c_s, whereas the differences for $S(k,\omega)$ at small-k values are more significant. Important discrepancies have been observed for the $F_{ep}(k,t)$ and $F_{ee}(k,t)$ calculated with the two potentials, but these properties cannot be experimentally determined. Although some properties calculated with the NPA potential are slightly closer to the experimental data, our results indicate that both potentials are able to reproduce the behavior of liquid lithium.

ACKNOWLEDGMENTS

This work has been supported by the EEC SCIENCE program under Contract No. SC1-CT91-0754. We also acknowledge support from the DGICYT of Spain (Grant Nos. PB92-0645 and PB90-0613-503). We especially thank H. Sinn for providing us with the x-ray data presented in this work and also for giving us the data files of Fig. 13 in the experimental count-rate form. We thank P.H.K. de Jong, P. Verkerk, and I.M. de Schepper for providing us with neutron scattering data and very helpful discussions. Finally, the supply of computer time from the CESCA is also acknowledged.

[1] M. Shimoji, *Liquid Metals* (Academic, London, 1977).
[2] W. van der Lugt and B.P. Alblas, in *Handbook of Thermodynamic and Transport Properties of Alkali Metals*, edited by R.W. Ohse (Blackwell, Oxford, 1985), Chap. 5.1.
[3] L.E. González, D.J. González, M. Silbert, and J.A. Alonso, J. Phys.: Condens. Matter **5**, 4283 (1993).
[4] M. Canales, J.A. Padró, L.E. González, and A. Giró, J. Phys.: Condens. Matter **5**, 3095 (1993).
[5] N.W. Ashcroft, Phys. Lett. **23**, 48 (1966).
[6] J. Hafner, *From Hamiltonians to Phase Diagrams* (Springer, Berlin, 1987).
[7] S. Ichimaru and K. Utsumi, Phys. Rev. B **24**, 7385 (1981).
[8] L.E. González, A. Meyer, M.P. Iñiguez, D.J. González, and M. Silbert, Phys. Rev. E **47**, 4120 (1993).
[9] P.H.K. de Jong, Ph.D. thesis, Technical University Delft, 1993.
[10] P.H.K. de Jong, P. Verkerk, and L.A. de Graaf, J. Non-Cryst. Solids **156-158**, 48 (1993); P.H.K. de Jong, P. Verkerk, and L.A. de Graaf, J. Phys.: Condens. Matter (to be published).
[11] E. Burkel, *Inelastic Scattering of X Rays with Very High Energy Resolution* (Springer, Berlin, 1991).
[12] P. Verkerk (private comunication).
[13] A.D.J. Haymet, Chem. Phys. Lett. **107**, 77 (1984).
[14] R.L. McGreevy and L. Pusztai, Proc. R. Soc. London Ser. A **430**, 241 (1990).
[15] U. Balucani and R. Vallauri, Chem. Phys. Lett. **166**, 77 (1990).
[16] M. Canales and J. A. Padró, Mol. Sim. **8**, 335 (1992).
[17] J.P. Hansen and I.R. McDonald, *Theory of Simple Liquids* (Academic, London, 1986).
[18] J.S. Murday and R.M. Cotts, Z. Naturforsch. A **26**, 85 (1971).
[19] M. Gerl and A. Bruson, in *Handbook of Thermodynamic and Transport Properties of Alkali Metals* (Ref. [2]), Chap. 7.5.
[20] M.P. Allen and D.J. Tildesley, *Computer Simulation of Liquids* (Clarendon, Oxford, 1987).
[21] C. Hoheisel and R. Vogelsang, Comput. Phys. Rep. **8**, 1 (1988).
[22] C. Hoheisel, R. Vogelsang, and M. Schoen, J. Chem. Phys. **87**, 7195 (1987).
[23] N.T. Ban, C.M. Randall, and D.J. Montgomery, Phys. Rev. **128**, 6 (1962).
[24] E.E. Shpil'rain, K.A. Yakimovich, V.A. Fomin, S.N. Skovorodjko, and A.G. Mozgovoi, in *Handbook of Thermodynamic and Transport Properties of Alkali Metals* (Ref. [2]), Chap. 7.3.
[25] J.P. Boon and S. Yip, *Molecular Hydrodynamics* (McGraw-Hill, New York, 1980).
[26] S. Kambayashi and G. Kahl, Phys. Rev. A **46**, 3255 (1992); Europhys. Lett. **18**, 421 (1992).
[27] K. Hornung, in *Handbook of Thermodynamic and Transport Properties of Alkali Metals* (Ref. [2]), Chap. 6.4.
[28] B.J. Berne and G.D. Harp, Adv. Chem. Phys. **17**, 63 (1970).
[29] I.M. de Schepper and M.H. Ernst, Physica A **98**, 189 (1979).
[30] P. Verkerk, Nuovo Cimento **12**, 441 (1990).
[31] G. Kahl, S. Kambayashi, and G. Nowotny, J. Non-Cryst. Solids **156-158**, 15 (1993).
[32] G. Wahnström and L. Sjögren, J. Phys. C **15**, 401 (1982).
[33] H. Sinn (private communication).
[34] I.M. de Schepper and E.G.D. Cohen, J. Stat. Phys. **27**, 223 (1982).
[35] I.M. de Schepper, P. Verkerk, A.A. van Well, and L. A. de Graaf, Phys. Rev. Lett. **50**, 974 (1983)
[36] L.E. González, D.J. González, and K. Hoshino, J. Phys: Condens. Matter **6**, 3849 (1994).
[37] Chr. Morkel and T. Bodensteiner, J. Phys.: Condens. Matter **2**, SA251 (1990).
[38] G. Jacucci and I.R. McDonald, Mol. Phys. **39**, 515 (1980).
[39] W.E. Alley and B. Alder, Phys. Rev. A **27**, 3158 (1983).
[40] I.M. de Schepper, E.G.D. Cohen, C. Bruin, J.C. van Rijs, W. Montfrooij, and L.A. de Graaf, Phys. Rev. A **38**, 271 (1988).